2014

Applications of tuned mass dampers to improve performance of large space mirrors

Yingling, Adam J.

Acta Astronautica, Volume 94, 2014, pp. 1-13.
http://hdl.handle.net/10945/44929

Acta Astronautica 94 (2014) 1–13

Contents lists available at ScienceDirect

Acta Astronautica

journal homepage: www.elsevier.com/locate/actaastro

Applications of tuned mass dampers to improve performance of large space mirrors ☆

Adam J. Yingling [a], Brij N. Agrawal [b,*]

[a] Naval Research Laboratory, Washington, DC 20375, USA
[b] Naval Postgraduate School, Monterey, CA 93943, USA

ARTICLE INFO

Article history:
Received 6 February 2013
Received in revised form
25 July 2013
Accepted 28 July 2013
Available online 17 August 2013

Keywords:
Smart structures
Tuned mass dampers
Imaging satellites
Adaptive optics
Active hybrid mirrors

ABSTRACT

In order for future imaging spacecraft to meet higher resolution imaging capability, it will be necessary to build large space telescopes with primary mirror diameters that range from 10 m to 20 m and do so with nanometer surface accuracy. Due to launch vehicle mass and volume constraints, these mirrors have to be deployable and lightweight, such as segmented mirrors using active optics to correct mirror surfaces with closed loop control. As a part of this work, system identification tests revealed that dynamic disturbances inherent in a laboratory environment are significant enough to degrade the optical performance of the telescope. Research was performed at the Naval Postgraduate School to identify the vibration modes most affecting the optical performance and evaluate different techniques to increase damping of those modes. Based on this work, tuned mass dampers (TMDs) were selected because of their simplicity in implementation and effectiveness in targeting specific modes. The selected damping mechanism was an eddy current damper where the damping and frequency of the damper could be easily changed. System identification of segments was performed to derive TMD specifications. Several configurations of the damper were evaluated, including the number and placement of TMDs, damping constant, and targeted structural modes. The final configuration consisted of two dampers located at the edge of each segment and resulted in 80% reduction in vibrations. The WFE for the system without dampers was 1.5 waves, with one TMD the WFE was 0.9 waves, and with two TMDs the WFE was 0.25 waves. This paper provides details of some of the work done in this area and includes theoretical predictions for optimum damping which were experimentally verified on a large aperture segmented system.

Published by Elsevier Ltd. on behalf of IAA.

1. Introduction

The Naval Postgraduate School (NPS) has received a 3-m diameter segmented mirror telescope (SMT) that uses active hybrid mirror (AHM) technology for the active control of segmented mirrors [1–3].

Before the system can be used operationally, the mirrors must be aligned to very tight tolerances. These mirrors are very lightweight and have low damping. As such, the relative motions between segments are more than a wavelength when exposed to the ambient conditions of a clean room. This is due to the dynamic excitation of segments caused by low level air pressure perturbations. The phase diversity (PD) sensor used for segment alignment is unable to perform as designed under such high magnitude perturbations due to dynamic range limitations. It is desirable to have the wavefront error (WFE) less than one-quarter waves for this sensor.

☆ This paper was presented during the 63rd IAC in Naples.

* Corresponding author. Tel.: +1 831 656 3338; fax: +1 831 656 3111.
E-mail addresses: Adam.Yingling@nrl.navy.mil (A.J. Yingling), agrawal@nps.edu (B.N. Agrawal).

0094-5765/$ - see front matter Published by Elsevier Ltd. on behalf of IAA.
http://dx.doi.org/10.1016/j.actaastro.2013.07.039

Research performed at the Naval Postgraduate School revealed several structural modes; however, the critical modes significantly contributing to WFE were between 26 Hz and 45 Hz. These are modes that create relative motion between the segments.

Although different techniques to increase damping of those modes were considered, tuned mass dampers (TMDs) were selected because of their simplicity in implementation and effectiveness in targeting specific modes. The selected damping mechanism was an eddy current damper where the damping and frequency of the damper could be easily changed. System identification of segments was performed to derive TMD specifications. Several configurations of the damper were evaluated, including the number and placement of TMDs, damping constant, and targeted structural modes.

Section 2 discusses details of the SMT, Section 3 discusses vibration modes contributing to WFE, Section 4 discusses TMD theory, Section 5 discusses modal mass approximation, Section 6 discusses experimental test results, Section 7, quantifies the vibration in terms of WFE, and Section 8 summarizes the results.

2. The segmented mirror telescope

The SMT shown in Fig. 1 is located at NPS and was the testbed for the work presented in this paper.

The primary mirror segments, secondary mirror, secondary tower, back-end optics, mounting ring and test frame are annotated in Fig. 1. The mounting ring allows the telescope to tilt up and down, and rotate about its optical axis, as annotated in Fig. 2.

The only optical elements in the optical train that contain curvature are the primary, secondary, and tertiary mirrors. As such, the SMT is considered a three mirror system. The other optical components in the optical train are flat mirrors and serve to redirect the light path to the image plane. The primary optic of the SMT consists of six actuated hybrid mirrors (AHMs).

The structure of each AHM is composed of a silicon carbide (SiC) substrate, to which a highly reflective nanolaminate is epoxied. The nanolaminate serves serves as the mirror face.

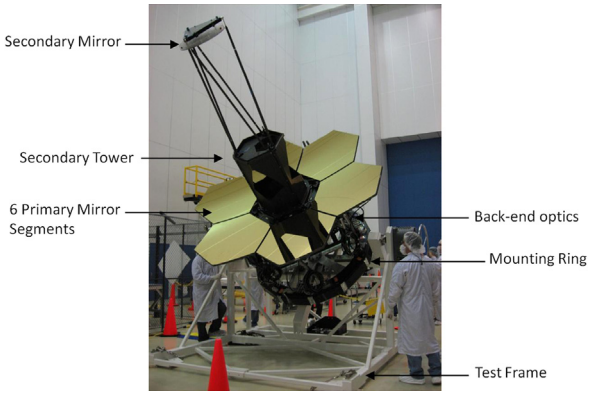

Fig. 1. The segmented mirror telescope (SMT).

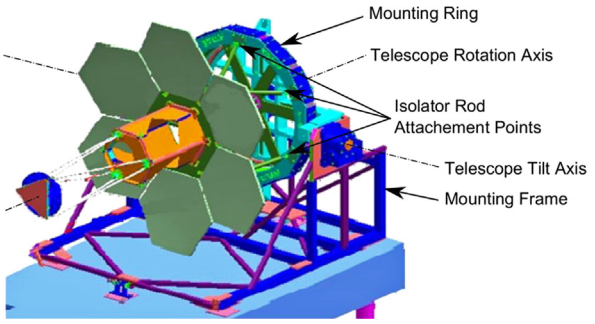

Fig. 2. Test frame rotation and tilt axes.

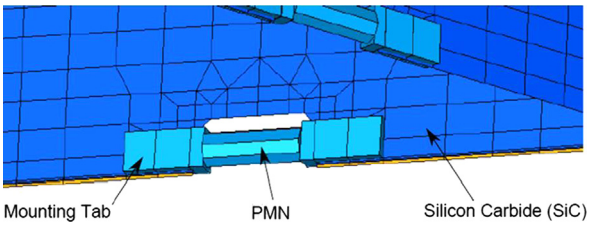

Fig. 3. Embedded face sheet actuator (FSA).

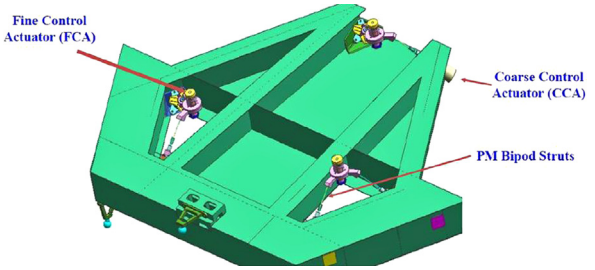

Fig. 4. The fine control actuators (FCAs) and coarse control actuators (CCAs). (For interpretation of the references to color in this figure legend, the reader is referred to the web version of this article.)

As shown in Fig. 3, face sheet actuators (FSAs) are embedded in the bottom of the SiC and serve to change the optical prescription of the segment.

The FSAs are composed of lead magnesium niobate (PMN) that expand when voltage is applied across them. Each SMT segment is embedded with 156 FSAs.

The SiC is supported at three locations by fine control actuators (FCAs) that move the segment in piston, tip, and tilt with nanometer and nanoradian precision. Each FCA is supported by two coarse control actuators (CCAs) in the bi-pod arrangement shown in Fig. 4.

Together the CCAs move the segments in all six degrees of freedom with micrometer and microradian precision. The CCAs are mounted to the precision support structure (PSS), shown green in Fig. 4.

3. Vibration induced WFE

Vibration-induced WFE is caused by dynamic motion of optical surfaces. Fig. 5 depicts a perturbed optic surface vibrating at an amplitude of $\partial Z(x)$.

The optical path difference (OPD) a light ray travels is twice this perturbation as it traverses this distance both before and after reflection.

There are many OPDs across the aperture, one for each ith pixel on the image plane. WFE is then defined as the standard deviation of all the non-zero OPDs,

$$\mathrm{WFE} = \sqrt{\frac{1}{N-1}\sum_{i=1}^{N}(OPD_i-\tau)^2} \quad \text{where} \quad \tau = \frac{1}{N}\sum_{i=1}^{N} OPD_i. \tag{1}$$

In this work, color scales were used such that large WFE values produced sharp contrasts, as seen in Fig. 6(a), and small WFE values are hard to distinguish from the background, as seen in Fig. 6(b). In Fig. 6 positive WFE is red in color, negative WFE is blue, and WFE of zero value is green.

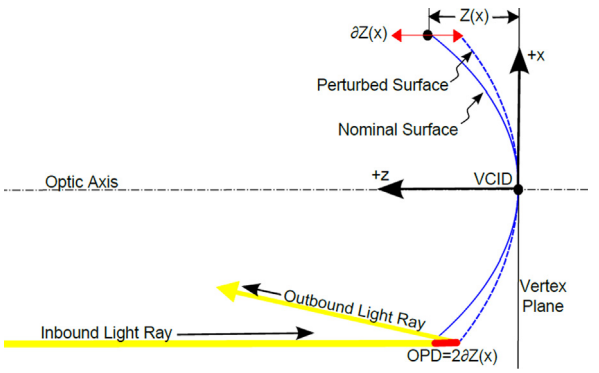

Fig. 5. Optical path difference (OPD).

Three modes shape types were seen during system identification tests; as shown in Fig. 7, they were (a) frame modes, (b) rocking modes, and (c) curvature modes.

The contribution of these modes to WFE is shown in Fig. 8, of which (b) the rocking modes are the primary contributor. Fig. 8 clearly indicates that of the three mode shape types, the critical modes requiring dampening are the rocking modes. These modes range from 26 Hz to 45 Hz, as shown in Fig. 9.

The rocking modes result due to flexibility in the latches connecting the PSS to the hex ring annotated in Fig. 10.

As discussed in [2,3], the rocking modes are predicted mode shapes in the finite element. Fig. 11 depicts the segments edge-wise, rocking about the latch, and approximates the mode as a beam rocking about the node point with a latch stiffness k_p.

Note that while none of the mass at the node point participates in this mode, all of the mass at other points participates with the maximum the outer edge of the segment. As such, the effective mass participating in this mode is a percentage of the total mass. This is called the modal mass m_p and can be used to idealize the rocking mode as the spring-mass system shown in Fig. 12.

The theory derived in the next section builds off of the idealization shown in Fig. 12.

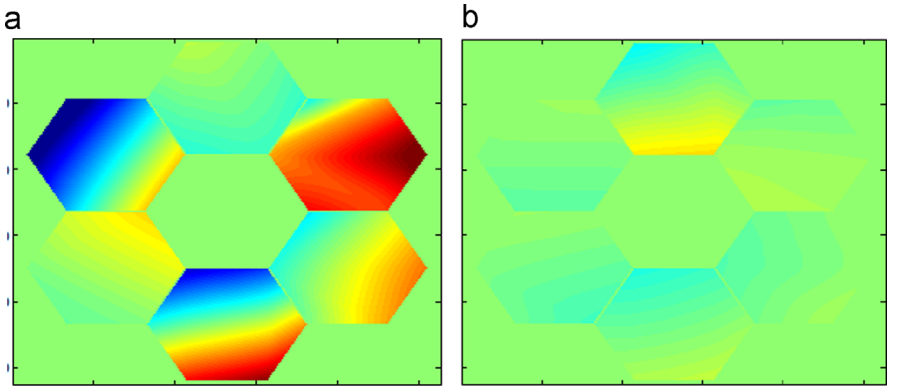

Fig. 6. Optical path difference (OPD) maps. (For interpretation of the references to color in this figure legend, the reader is referred to the web version of this article.)

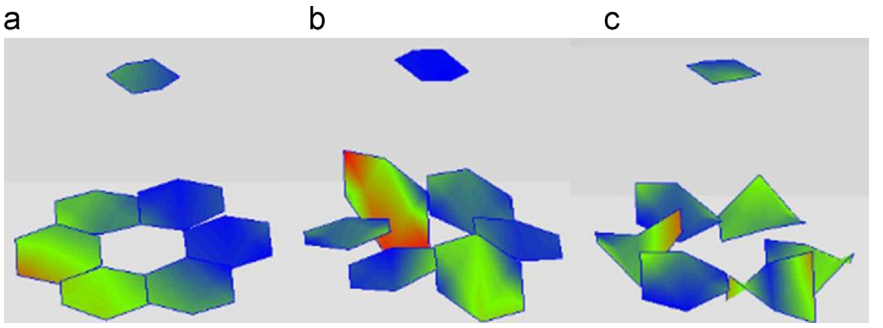

Fig. 7. SMT mode shape types. (a) Frame modes, (b) rocking modes and (c) curvature modes.

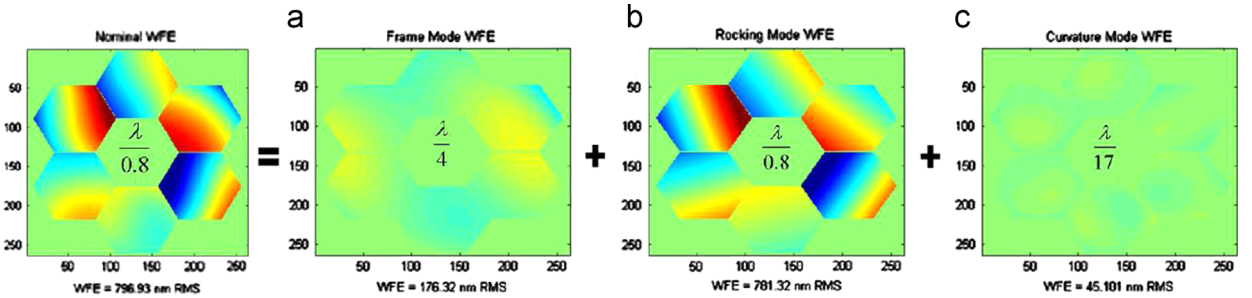

Fig. 8. The total wavefront error (WFE) induced by (a) frame modes (b) rocking modes and (c) curvature modes.

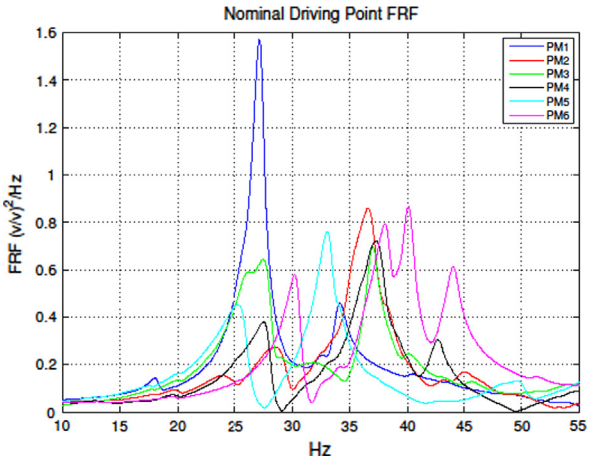

Fig. 9. Frequency response functions (FRFs) of the primary mirror (PM) segments.

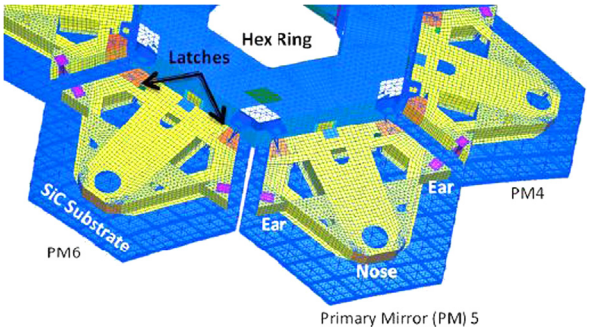

Fig. 10. Segment latch locations.

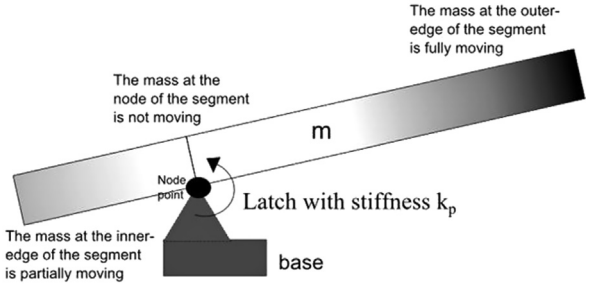

Fig. 11. Rocking mode approximation.

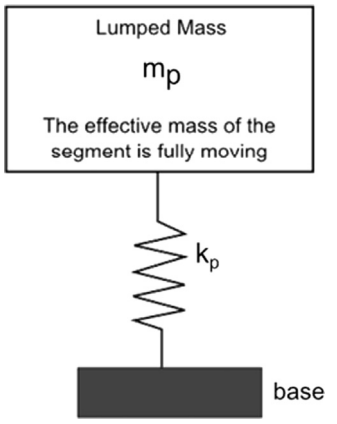

Fig. 12. Rocking mode idealization.

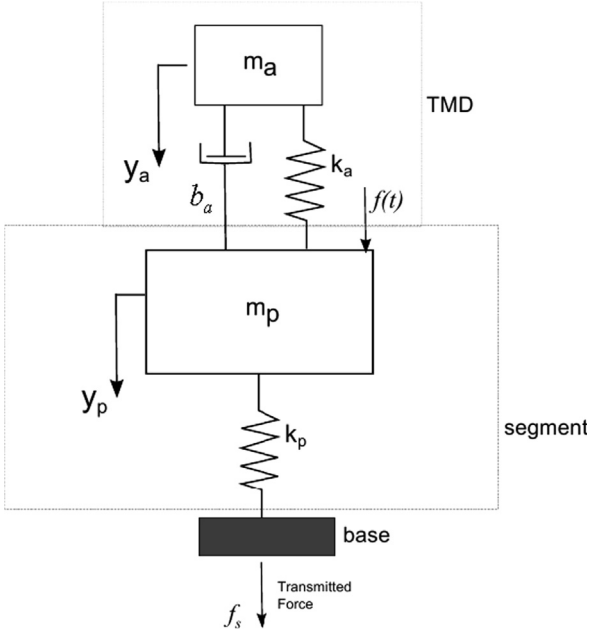

Fig. 13. Rocking mode idealization with TMD.

4. Tuned mass damper theory

A TMD can be idealized as a spring-mass-damper added to the existing system. This is shown in Fig. 13.

As shown in Fig. 13, a disturbing force $f(t)$ is perturbing the system, causing a vertical displacement of the segment y_p and vertical displacement of the TMD y_a. The disturbing force also causes a transmitted force f_s.

The equation of motion for the segment is

$$m_p\ddot{y}_p + k_p y_p - \bar{k}_a(y_a - y_p) = f(t), \tag{2}$$

and the equation of motion for the TMD is

$$m_a\ddot{y}_a + \bar{k}_a(y_a - y_p) = 0, \tag{3}$$

where for convenience, the stiffness and damping components have been written together as

$$\bar{k}_a = k_a + j\omega b_a, \tag{4}$$

and ω is the disturbance frequency.

The objective of adding a TMD to a segment is to reduce the response of the segment to $f(t)$. Mathematically this is shown by taking the laplace transform,

$$L\{h(t)\} \equiv \int_0^\infty h(t)e^{-st}dt, \tag{5}$$

of the TMD equation of motion in Eq. (3) and rewriting it as

$$L\{m_a\ddot{y}_a + \bar{k}_a y_a = \bar{k}_a y_p\} \Rightarrow (\bar{k}_a - \omega^2 m_a)Y_a(s) = \bar{k}_a Y_p(s) \tag{6}$$

In Eq. (6) it is evident that if one properly selects the stiffness k_a and mass m_a of the TMD for a given disturbing frequency ω, then the terms inside the parentheses would cancel each other. Due to equivalence, the right hand side of the equation then requires that the segment displacement y_p also be zero.

The blue dashed line in Fig. 14 shows the nominal response of the segment without TMDs.

The non-dimensional parameters used in Fig. 15 include the dimensionless disturbing frequency,

$$g \equiv \frac{\omega}{\omega_p}, \tag{7}$$

where the resonant frequency of the segment is

$$\omega_p \equiv \sqrt{\frac{k_p}{m_p}}. \tag{8}$$

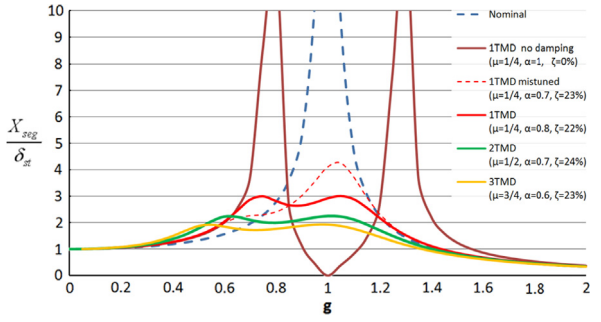

Fig. 14. Segment responses for various TMD configurations. (For interpretation of the references to color in this figure legend, the reader is referred to the web version of this article.)

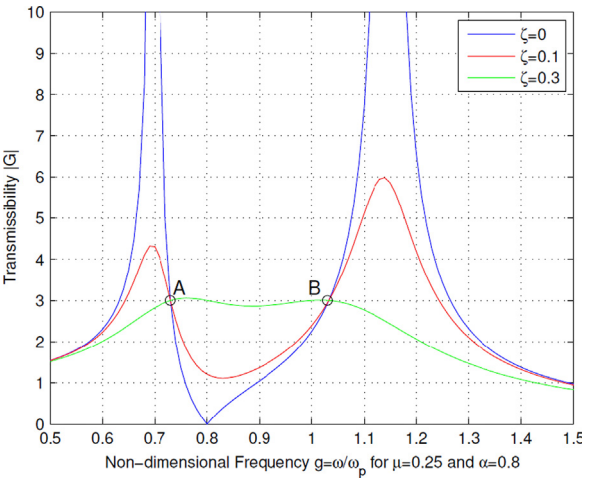

Fig. 15. Transmissibility curves.

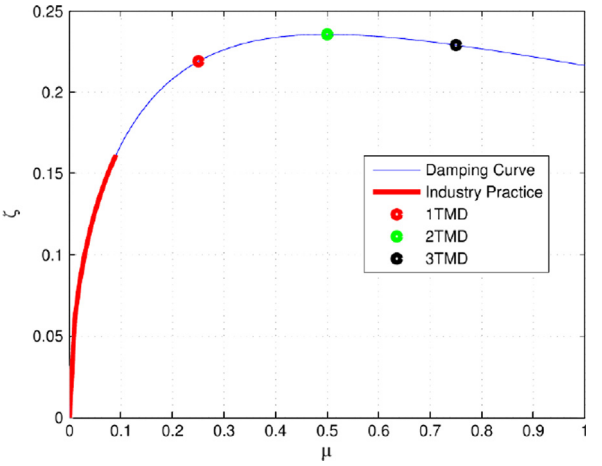

Fig. 16. Damping ratio as a function of mass ratio.

The TMD damping is defined as

$$\zeta \equiv \frac{b_a}{2\sqrt{k_a m_a}}. \tag{9}$$

The mass ratio is defined as

$$\mu \equiv \frac{m_a}{m_p}. \tag{10}$$

The frequency ratio is defined as

$$\alpha \equiv \frac{\omega_a}{\omega_p}, \tag{11}$$

where the resonant frequency of the TMD is

$$\omega_a \equiv \sqrt{\frac{k_a}{m_a}}. \tag{12}$$

Fig. 15 shows that by adding a TMD, a degree of freedom has been added to the system. Thus two resonant frequencies exist where before there was only mode at $g=1$. The other curves in Fig. 16 show that by varying μ, α, and ζ, the response of the segment can be affected.

The parameters in Eqs. (9)–(11) can be designed to optimize the amount of damping imparted to the system. To do this, the transfer function of the disturbing force to the transmitted force is defined as

$$G(\omega) \equiv \frac{f_s}{f(t)}. \tag{13}$$

As shown in [3,4], rewriting Eq. (13) in terms of the non-dimensional parameters is accomplished by taking the Laplace of Eqs. (2) and (3) and rewriting them into matrix form, which yields

$$\begin{bmatrix} k_p+\bar{k}_a-\omega^2 m_p & -\bar{k}_a \\ -\bar{k}_a & \bar{k}_a-\omega^2 m_a \end{bmatrix} \begin{bmatrix} y_p \\ y_a \end{bmatrix} = \begin{bmatrix} f \\ 0 \end{bmatrix}, \tag{14}$$

where the forcing function f is assumed to oscillate at a single frequency ω such that it is a constant in the Laplace domain.

Solving (14) for the displacements y_p and y_a simultaneously yields

$$\begin{bmatrix} y_p \\ y_a \end{bmatrix} = \frac{1}{\Delta} \begin{bmatrix} \bar{k}_a-\omega^2 m_p & \bar{k}_a \\ \bar{k}_a & k_p+\bar{k}_a-\omega^2 m_p \end{bmatrix} \begin{bmatrix} f \\ 0 \end{bmatrix}, \tag{15}$$

where Δ is

$$\Delta = (k_p+\bar{k}_a-\omega^2 m_p)(\bar{k}_a-\omega^2 m_a)-\bar{k}_a^2 = m_p m_a \omega^4 - [\bar{k}_a(m_p+m_a)+\bar{k}_a m_a]\omega^2 + k_p \bar{k}_a. \tag{16}$$

considering that the transmitted force f_S shown in Fig. 13 is

$$f_s = k_p \times y_p, \tag{17}$$

The non-dimensional transfer function $G(\omega)$ can be written as

$$G(\omega) = \frac{f_s}{f} = \frac{k_p y_p}{f} = \frac{k_p}{\Delta}\left(\bar{k}_a-\omega^2 m_a\right). \tag{18}$$

Substituting Eq. (4) into (18) and writing Δ (16) out explicitly yields

$$G(\omega) = \frac{k_p(k_a+j\omega b_a-\omega^2 m_a)}{m_p m_a \omega^4 - [(k_a+j\omega b_a)(m_p+m_a)+k_p m_a]\omega^2 + k_p(k_a+j\omega b_a)}. \tag{19}$$

Non-dimensionalizing (19) by substituting in Eqs. (7)–(11) yields

$$G(g) = \frac{\alpha^2-g^2+2j\zeta\alpha g}{g^4-[(\alpha^2+2j\zeta\alpha g)(1+\mu)+1]g^2+(\alpha^2+2j\zeta\alpha g)}. \tag{20}$$

Fig. 16 shows Eq. 20 for various amounts of damping.

As described in [3,4], by noting that all the curves in Fig. 15 pass through points A and B, the dependence of the frequency ratio on the mass ratio can be derived,

$$\alpha = \frac{1}{1+\mu}. \tag{21]}$$

Also described in [3,4], optimum damping is found to be dependent on μ by noting that the transmissibility is minimized when points A and B are also the locations of peak response such that a line with zero slope can be drawn between them. This yields

$$\zeta^2 = \frac{3\mu}{8(1+\mu)^3}. \tag{22}$$

Noting that the only dependent variable is μ, it becomes important to select the optimum mass ratio, which is found by setting the derivative of Eq. (22) to zero and solving for μ,

$$\frac{\partial \zeta^2}{\partial \mu} = \frac{3}{8}(1+\mu)^{-3} - \frac{9\mu}{8}(1+\mu)^{-4} = 0 \tag{23a}$$

$$\mu_{opt} = \frac{1}{2}. \tag{23b}$$

A comparison of the mass ratios used for this research with those used in industry is shown in Fig. 16. Note that the optimum mass ratio is well above what is typically used in industry.

Eq. (22b) reveals that accurately predicting the modal mass m_p of the segment rocking mode is of utmost importance. Predicting the modal mass is discussed in the next section.

5. Modal mass approximation

Rayleigh's method [3,5] was used to determine the modal mass of the rocking mode. This method requires approximating the small Z-axis displacement of the segment in both space and time,

$$z(x,t) = \tilde{z}(x)\sin(\omega_n t+\phi) \tag{23}$$

where $\tilde{z}(x)$ is a shape function and $z(x,t)$ assumes oscillatory motion with a natural frequency of ω_n. Figs. 17 and 18

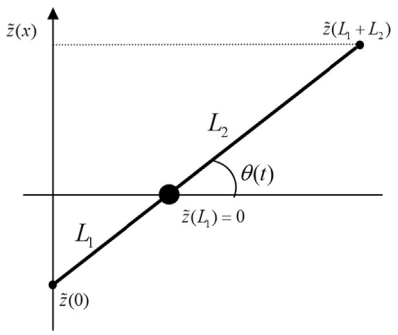

Fig. 17. Rocking mode description (side view).

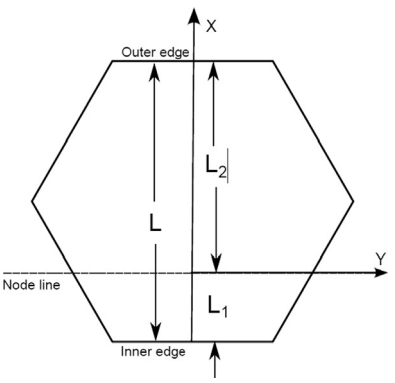

Fig. 18. Rocking mode description (top view).

depict the rocking mode of the segment and introduces parameters used to derive $\tilde{z}(x)$.

The rocking mode is characterized by the following boundary conditions,

$$\tilde{z}(0) = -L_1 \sin\ \theta \tag{24}$$

$$\tilde{z}(L) = \tilde{z}_{\max} = L_2 \sin\theta \tag{25}$$

$$\tilde{z}(L_1) = 0 \tag{26}$$

$$\tilde{z}'(x) = \text{constant} \tag{27}$$

$$\tilde{z}''(x) = 0 \tag{28}$$

As shown in [3], a solution to these boundary conditions is

$$\tilde{z}(x) = \frac{x}{L_2} - \frac{L_1}{L_2} \tag{29}$$

which is unitless because it has been normalized such that the maximum displacement at the outer edge is 1.

To find the modal mass, the general form of the kinetic energy equation is used,

$$T \equiv \frac{1}{2} m V^2. \tag{30}$$

The time derivative of Eq. (23) is

$$V(x,t) = \dot{z}(x,t) = \tilde{z}(x)\omega_n \times \cos(\omega_n t + \phi). \tag{31}$$

Writing the kinetic energy Eq. (30) in terms of Eq. (31) yields

$$T(x,t) \equiv \frac{1}{2} m(x) V^2(x,t), \tag{32}$$

where the mass is allowed to vary across the segment.

To find the total kinetic energy, Eq. (32) must be integrated across the segment,

$$T^{total}(t) \equiv \frac{1}{2} \int_0^L \gamma \times V^2(x,t) dx, \tag{33}$$

where the mass is assumed to be evenly distributed,

$$\gamma = m(x) = \frac{m}{L}. \tag{34}$$

As shown in [3], substituting Eq. (31) into Eq. (33) and simplifying yields

$$T^{total} = \frac{1}{2} \left(\int_0^L \gamma \times \tilde{z}^2(x) dx \right) \omega_n^2 \cos^2(\omega_n t + \phi), \tag{35}$$

where the term inside the brackets is the modal mass m_p, and the term outside the brackets is the normalized velocity $\tilde{V}(t)$ squared. This can be written as

$$T^{total} = \frac{1}{2} (m_p) \tilde{V}^2(t), \tag{36}$$

where

$$m_p = \int_0^L \gamma \times \tilde{z}^2(x) dx, \tag{37}$$

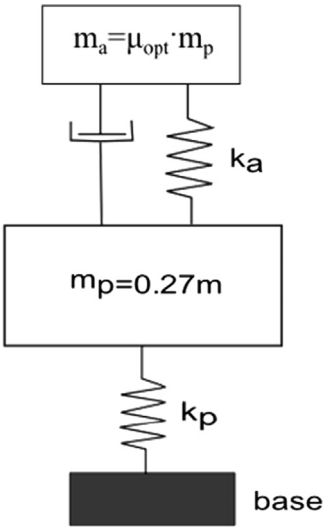

Fig. 19. Modal and TMD mass relations.

and

$$\tilde{V}(t) = \omega_n \cos(\omega_n t + \phi). \tag{38}$$

Substituting Eq. (29) into Eq. (37) and integrating yields

$$m_p = \int_0^L \gamma \times \left[\frac{x}{L_2} - \frac{L_1}{L_2} \right]^2 dx = m \left[\frac{L^2}{3L_2^2} - \frac{L}{L_2} + 1 \right], \tag{39}$$

where both Eq. (29) and $L_1 = L - L_2$ were substituted into Eq. (39).

Given that $L = 1$ m and $L_2 = 0.8$ m, Eq. (39) reduces to

$$m_p = m \left[\frac{1^2}{3(0.8)^2} - \frac{1}{0.8} + 1 \right] = 0.27\ \text{m}. \tag{40}$$

thus, for a segment weighing 29 lbs, the modal mass is

$$m_p = 0.27(29\ \text{lbs}) = 8\ \text{lbs}, \tag{41}$$

and the optimum TMD weight is found using Eqs. (10) and (17),

$$m_a = \mu_{opt} m_p = \frac{1}{2} 8\ \text{lbs} = 4\ \text{lbs}. \tag{42}$$

The results of this section are summarized in Fig. 19.

6. Experimental test results

Initial testing was accomplished on one segment. The test setup is shown in Fig. 20.

An impact hammer instrumented with a force transducer was used to input impulse excitations into the system. The impact location is annotated in Fig. 20. Seismic accelerometers sensitive to 1000 mV/g were placed around the segment to measure its response. These instruments are shown in Fig. 21.

As indicated in Fig. 20, various TMD locations and configurations were tested. Each TMD was 2 lbs in weight. The mass ratios for each TMD configuration are given in Table 1. Note that the optimum mass ratio is found in the 2 TMD configuration.

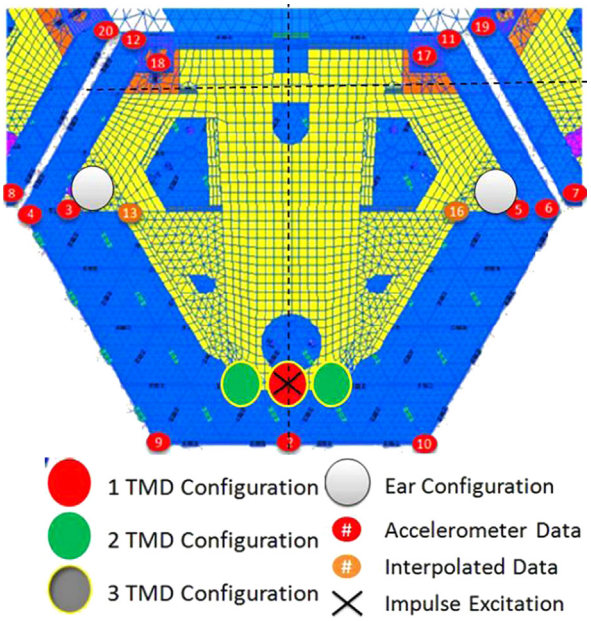

Fig. 20. One segment test setup.

Fig. 21. Impact hammer and tri-axial accelerometer (not to scale).

Table 1
Mass ratios for TMD configurations.

# of TMDs	μ
0	0
1	¼
2	½
3	¾

As shown in Fig. 22, over thirty configurations were tested for segment 5.

For each configuration in Fig. 20, the TMDs were tuned according to their mass ratios, as given in Eqs. (15) and (16).

The magnetic TMDs are shown in Fig. 23. Fig. 23(a) shows the outer-casing of the TMD which houses copper windings. The inner-core of the TMD is depicted in Fig. 23 (b) of the same figure and shows a magnetic core connected to the outer-casing by three flexures. Fig. 23(c) depicts that the relative motion between the inner-core and outer-casing produces eddy currents, which dampen the motion.

Tuning was accomplished by changing the flexure lengths of the springs. As depicted in Fig. 24(b), the flexures were slotted and attached to the outer-casing of the TMD using bolts. By loosening the bolts, twisting the

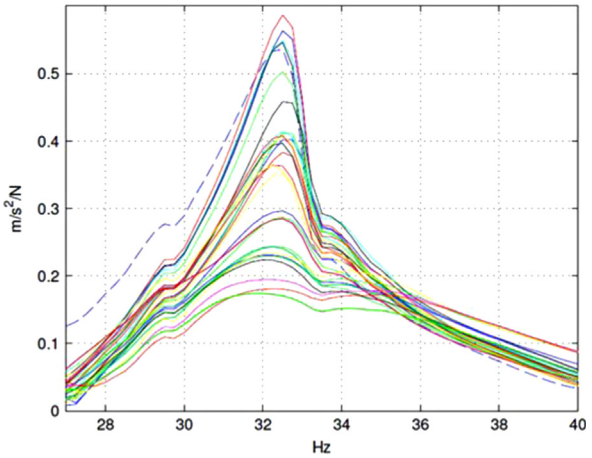

Fig. 22. All TMD configurations for segment 5.

outer-casing, and re-tightening, the effective length of the spring can be changed, changing the resonant frequency of the TMD. Noting that the flexure is essentially a cantilevered beam, the stiffness of the TMD is

$$k_a = \frac{3EI}{L^3}, \tag{43}$$

where E is the modulus of elasticity, I is the cross-section moment of inertia, and L is the effective length of the spring.

Before placed on the SMT, the TMD is tuned atop a shaker, such that the transmissibility curve indicates the resonance ω_a and damping $\zeta$of the TMD. An example is shown in Fig. 24.

In addition to the number of TMDs, TMD locations, TMD stiffness, TMD damping and targeted modes were all varied. All segments were tested in similar manner. Five configurations are summarized in Fig. 25 for a resonance at 33.5 Hz.

The dashed blue line is the nominal or 0TMD configuration with a non-dimensional resonance at 1,

$$\frac{\omega}{\omega_n} = \frac{2\pi \times 33.5\ \text{Hz}}{2\pi \times 33.5\ \text{Hz}} = 1. \tag{44}$$

The solid blue line is the 1TMD with a slightly mistuned TMD at 25 Hz. Note that according to Eq. (20), the frequency ratio should be

$$\alpha = \frac{1}{1+1/4} = \frac{4}{5}, \tag{45}$$

which, according to Eq. (11), requires tuning the TMD to

$$f_a = \frac{\omega_a}{2\pi} = \frac{\alpha \times \omega_b}{2\pi} = \frac{4}{5} \times \frac{(2\pi \times 33.5\ \text{Hz})}{2\pi} = 27\ \text{Hz} \tag{46}$$

As shown by the solid red curve in Fig. 25, properly tuning the 1TMD configuration to 27 Hz further reduces the response.

The 2TMD configuration shown by the solid green curve in Fig. 25 provides the optimum damping, verifying the predictions given in Eq. (22b).

Given the success on one segment, TMDs were implemented on all the segments. To test these configurations,

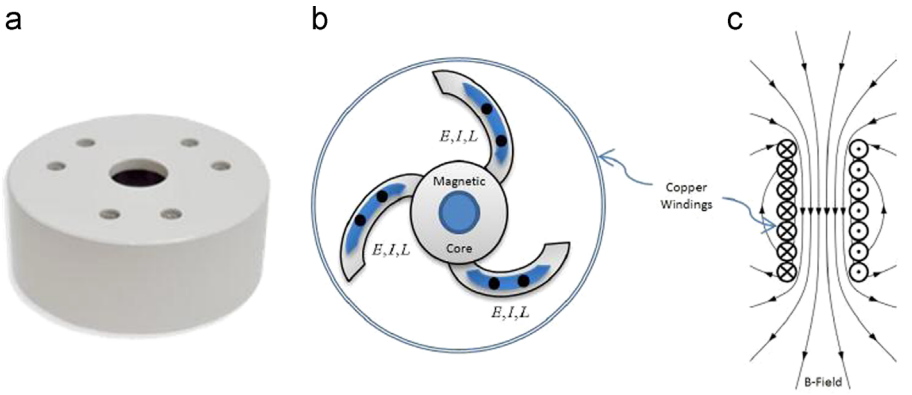

Fig. 23. The magnetic tuned mass damper (TMD).

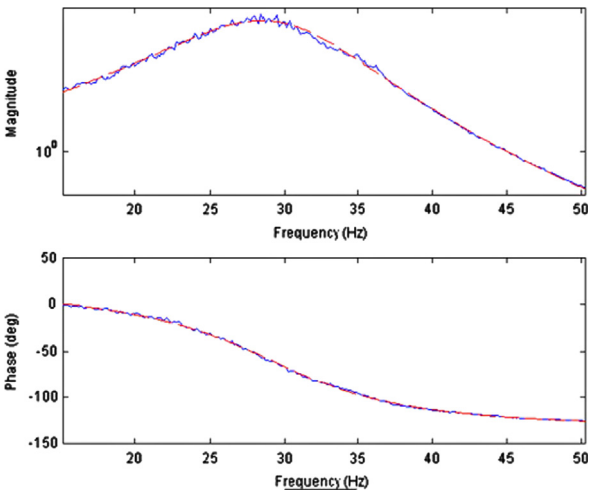

Fig. 24. TMD transmissibility curve.

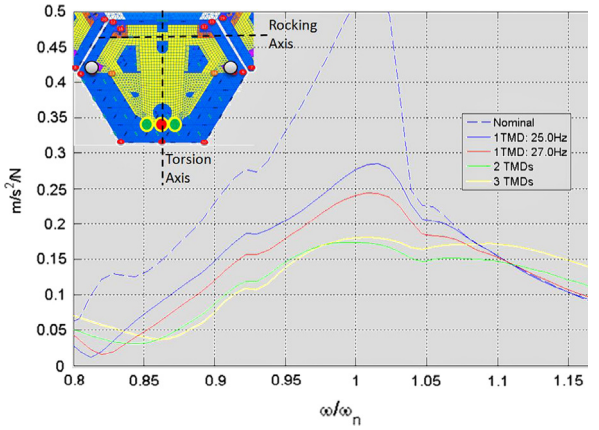

Fig. 25. Select TMD configuration for segment 6. (For interpretation of the references to color in this figure legend, the reader is referred to the web version of this article.)

it was impractical to instrument accelerometers on all segments simultaniously. Instead, a laser-vibrometer was used. This setup is shown in Fig. 26.

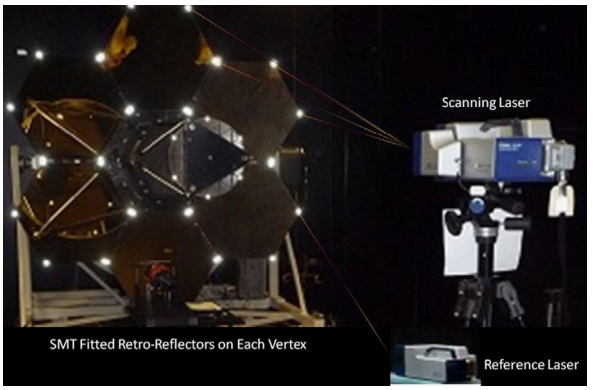

Fig. 26. Laser vibrometer test setup.

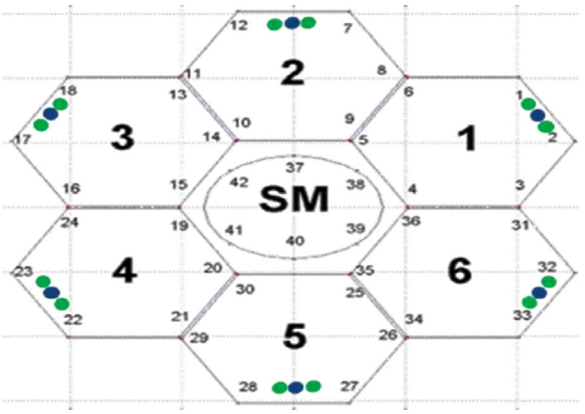

Fig. 27. Laser vibrometer test index. (For interpretation of the references to color in this figure legend, the reader is referred to the web version of this article.)

As seen in Fig. 26, the vertex of each segment was fitted with retro-reflectors to provide high-quality laser return signatures to the scanning laser.

As indicated in Fig. 27, only the 0, 1, and 2TMD configurations were tested this time; however, TMDs were mounted to all of the segments.

The blue circles in Fig. 27 indicate the 1TMD configuration. The green circles indicate the 2TMD configuration.

The numbering on the segment vertices are the index values used throughout the test.

As described previously, an impact hammer was used to excite the structure; however, instead of using accelerometers to measure the response, vibrations amplitudes were calculated using Doppler shifts in the return signature of the laser emitted from the scanning head of the laser vibrometer. This is shown in Fig. 28.

The "vibrating plate" annotated in Fig. 28 represents the retro-reflectors on the segment vertices. The "input signal" originates from the force tranducer of the impact hammer that is providing the excitation.

Also indicated in Fig. 28, many fast Fourier transform (FFT) analyses were produced during the testing and include auto spectral density (ASD), power spectral density (PSD), and frequency response functions (FRFs). The spectral resolution for this testing was ¼ Hz per line,

$$\Delta f = \frac{200\ \text{Hz}}{800\text{lines}} = \frac{1}{4}\ \text{Hz/line} \tag{47}$$

The displacement response for the first index point is shown in Fig. 30 for the nominal (0TMD), 1TMD, and 2TMD configurations.

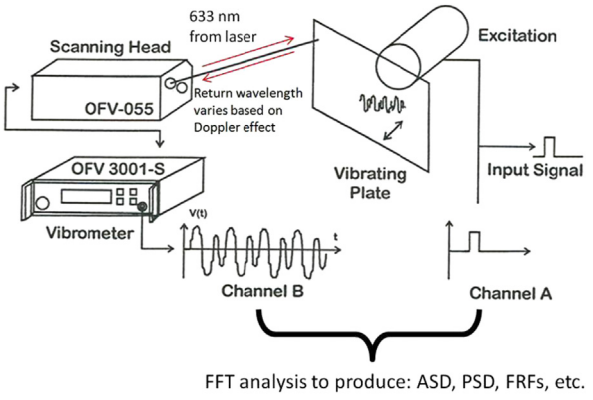

Fig. 28. Laser vibrometer equipment.

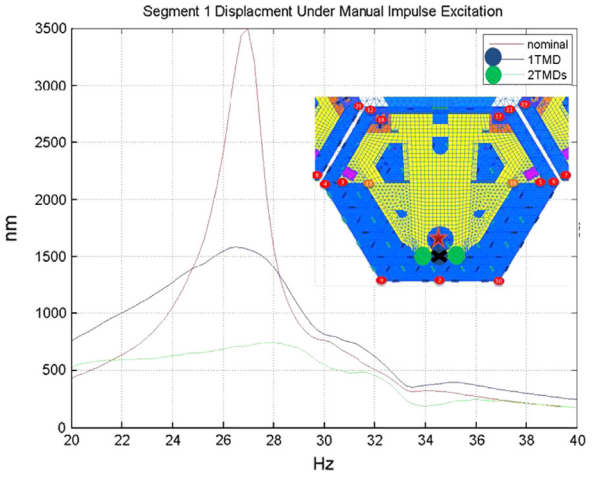

Fig. 29. Index 1 impulse displacement response. (For interpretation of the references to color in this figure legend, the reader is referred to the web version of this article.)

As annotated in Fig. 29, the impact location is marked with an "X" and is the same location used for the single segment testing described previously. However, the response was measured on the front side of the mirror at the location indicated by the star.

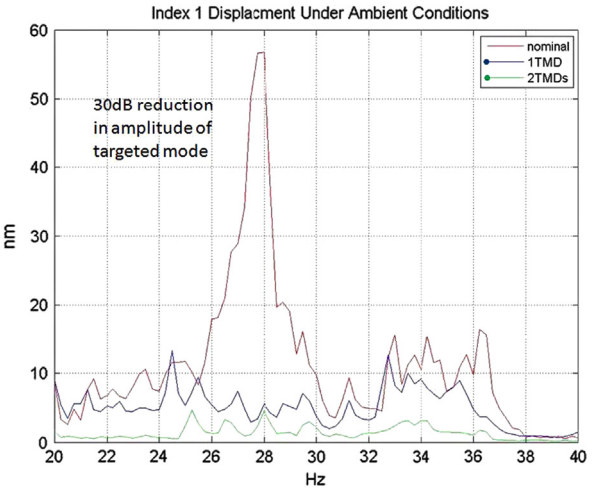

Fig. 30. Index 1 ambient displacement response. (For interpretation of the references to color in this figure legend, the reader is referred to the web version of this article.)

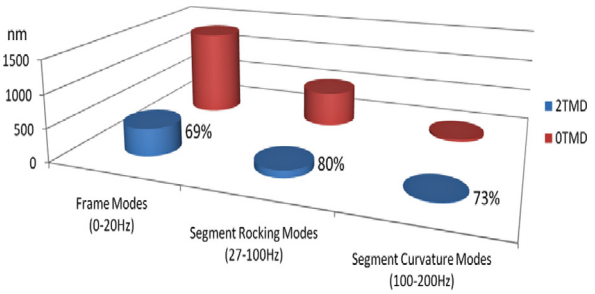

Fig. 31. TMD vibration amplitude reduction.

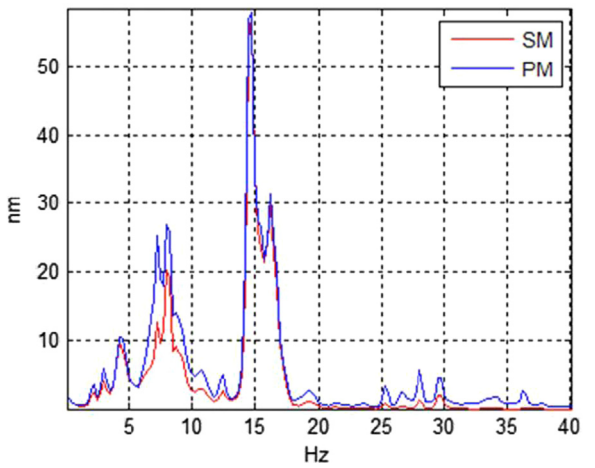

Fig. 32. The frame modes (0–20 Hz).

Shown as a solid red curve in Fig. 29, the nominal response to an impulse excitation is 3.5 microns. This response is significantly reduced to 1.5 microns with 1TMD, shown as a solid blue curve. The 2TMD configuration virtually eliminates the resonant mode all-together with amplitudes less than 0.5 microns.

After tuning and impact testing, operational deflection shapes (ODS) were captured using the reference laser shown in Fig. 27. For this testing, no excitation was applied to the segments. Instead, the response of the segment as it was perturbed by the ambient environment was recorded. The results for index point 1 are shown in Fig. 31.

Note that the amplitudes in Fig. 30 are much smaller than the amplitudes in Fig.29. This is because the ambient excitation sources only provide small perturbations. The solid red curve in Fig. 30 shows the nominal response of the segment. As before, the 1TMD configuration, the solid blue curve, significantly reduces the problem mode.

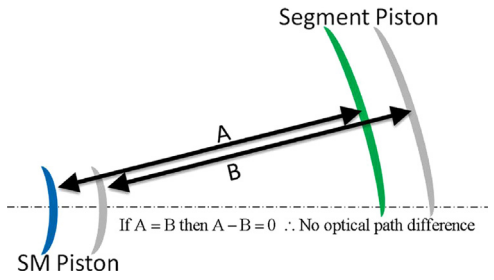

Fig. 33. Frame modes move all optics identically.

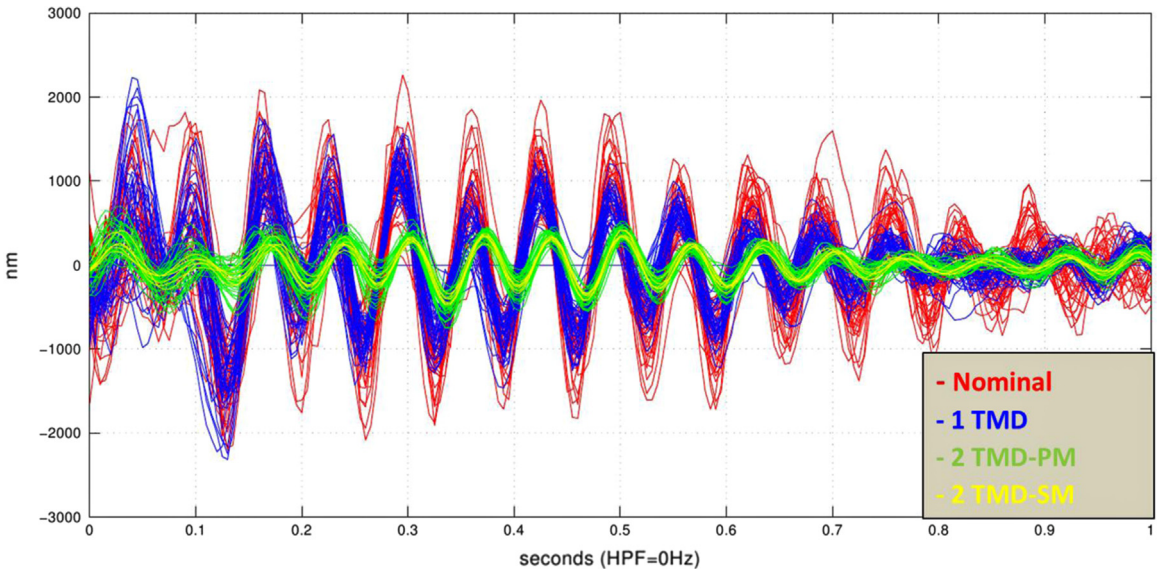

Fig. 34. The SMT time-domain response. (For interpretation of the references to color in this figure legend, the reader is referred to the web version of this article.)

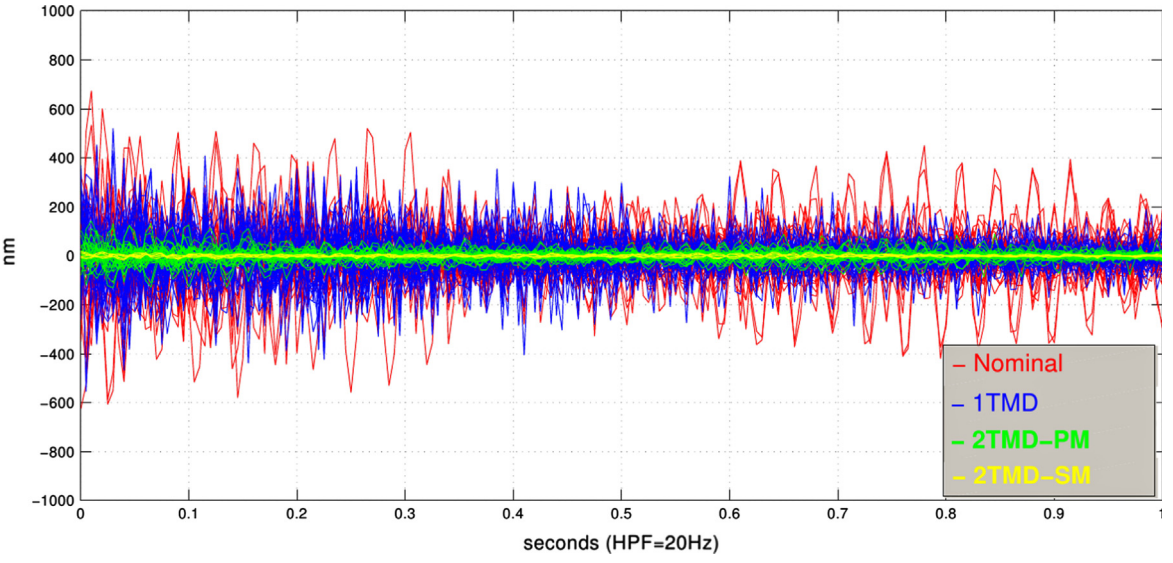

Fig. 35. The SMT time-domain response with frame modes removed. (For interpretation of the references to color in this figure legend, the reader is referred to the web version of this article.)

The 2TMD configuration performs even better and has a nice broadband effect that also dampens adjacent modes.

Averaging the results of all the test indices, it was found that the vibration amplitudes of the rocking modes were reduced by 80%. Although not targeted, the frame modes, and curvature modes were also significantly reduced. These results are summarized in Fig. 31.

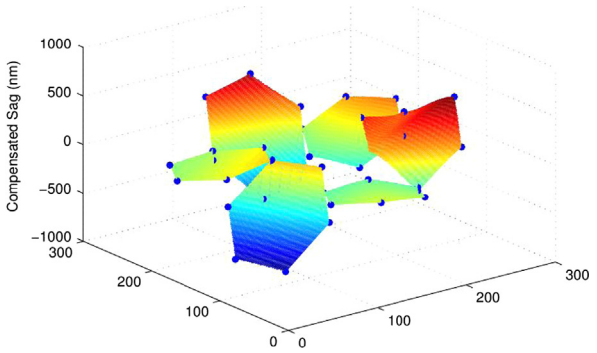

Fig. 36. Interpolation between test indices. (For interpretation of the references to color in this figure legend, the reader is referred to the web version of this article.)

7. Quantifying wavefront error

As can be seen in Fig. 32, the frame modes below 20 Hz are large in magnitude with regard to the rocking modes near 30 Hz.

Further, Fig. 32 shows that the secondary mirror (SM) amplitudes are equivalent in magnitude to the primary mirror (PM) amplitudes.

It can also be seen that the PM and SM optics are moving in phase with each other, as shown in Fig. 33. Thus for the frame modes, the optical path lengths between the PM and SM are not changing. This is depicted in Fig. 34.

The curves in Fig. 34 were generated by transforming the spectral data presented previously into the time-domain using the Fourier transform,

$$x(t_k) = \sum_{n=1}^{N} X(f_n) e^{i2\pi nk/N}, \tag{48}$$

for N discrete time samples.

The result of the Fourier transform, as shown in Fig. 34, shows that the SM data, shown as yellow curves, are in phase with the PM data, shown as green curves. Note that this is because the 15 Hz frame mode is dominating the results. Fig. 36 shows the frame modes filtered from the data, then Fourier transformed.

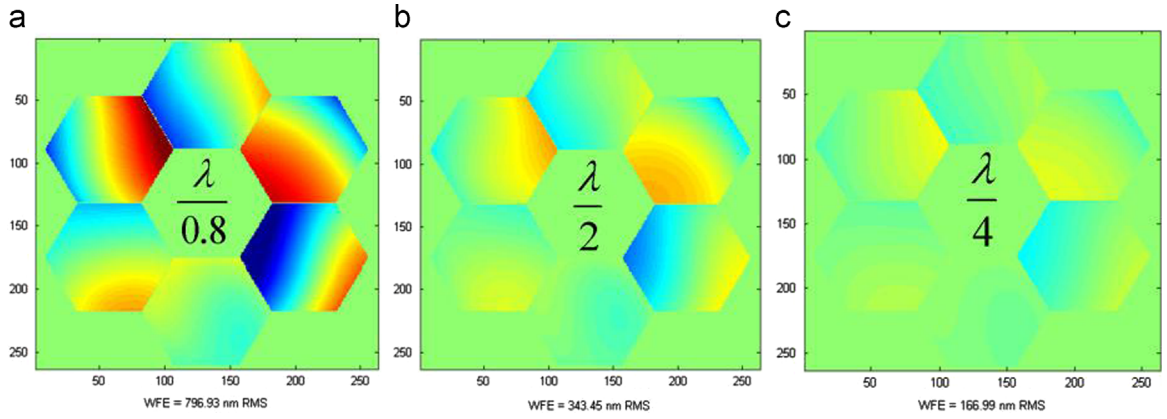

Fig. 37. a, b, c: 0TMD, 1TMD, and 2TMD OPD maps.

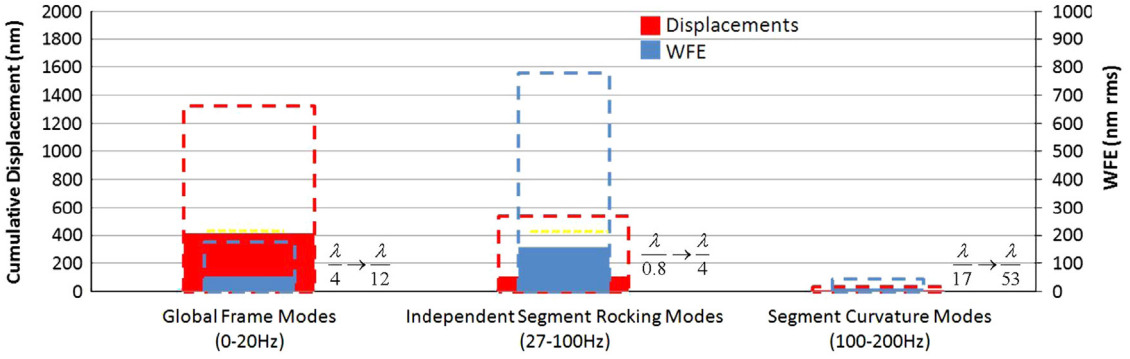

Fig. 38. Vibration amplitudes (left ordinate) and associated WFE (right ordinate). (For interpretation of the references to color in this figure legend, the reader is referred to the web version of this article.)

Fig. 35 indicates relative motion between the SM, shown as the yellow curve, and the PM, shown as the green curve, as the curves are no longer in phase with each other.

It is the relative motion between optics that causes WFE. Thus it is necessary to remove the frame modes to quantify WFE.

The next step becomes to estimate the displacements across the entire aperture, not just at the test indices indicated in Fig. 27. This was accomplished by interpolating displacement values across each segment from the data existing at test indices. An example of this is shown in Fig. 36 for the nominal configuration; text indices are annotated as blue circles.

The results of the procedure described above generated the OPD maps shown in Fig. 37 for each configuration: nominal (0TMD), 1TMD, and 2TMD.

Fig. 37 shows that the WFE was reduced from 1.25 waves, $\lambda/0.8$, to 0.25 waves, $\lambda/4$. This is a reduction of a factor of 5 and should allow for testing to be conducted on the SMT that was previously not possible to the magnitude of the vibrations.

8. Conclusions

This work revealed that the segment rocking modes were the primary modes contributing to WFE. Additionally, theoretical predictions were given to optimize the reduction of these modes using TMDs. To do so, the modal mass was approximated to be 27% of the total mass of the segment and the optimum TMD mass was predicted to be half of the modal mass. These results were experimentally verified.

Further, implementation of the optimized TMDs resulted in reduction in vibration amplitudes by 80% and a reduction of WFE by a factor of 5.

These results are summarized in Fig. 38. The vibration displacements are shown in red and their magnitudes are on the left ordinate. The associated WFE with the vibrations are shown in blue and their magnitudes are on the right ordinate. The dashed lines in Fig. 38 indicate the nominal configuration and the solid line indicates the 2TMD configuration.

Acknowledgements

The authors would like to sincerely acknowledge the contribution of the members of NPS Spacecraft Reserarch and Design Center (SRDC) and the Adaptive Optics Center of Excellence (AOCoE). Research presented in this work was also conducted in collaboration with the Air Force Institute of Technology (AFIT), CSA Engineering, a Moog company, and Boeing SVS.

References

[1] G. Hickey, M. Ealey, D. Redding, Actuated hybrid mirrors for space telescopes, SPIE 7731 (2010) 773120–773121.
[2] A.J., Yingling, B.N., Agrawal, Applications of active optics in large space mirrors, in: Proceeding of 62nd International Astronautical Congress, 27 Sepember-1 October, 2011, Capetown, South Africa, IAC-11.C2.5.1.
[3] A.J., Yingling, Integrated Structures, Optics, and Controls for the Segmented Mirror Telescope, Naval Postgraduate School, Ph.D. Dissertation, September, 2012, Monterey, CA.
[4] Clarence W. de Silva, Vibration and Shock Handbook, first ed. CRC Press, 2005.
[5] W.T. Thomson, Theory of Vibration with Applications, Prentice Hall, 1997.